The Stomatopod Telson: Convergent Evolution in the Development of a Biological Shield

N. A. Yaraghi, M. Zhernenkov

DISCLAIMER

The Stomatopod Telson: Convergent Evolution in the Development of a Biological Shield

Nicholas A. Yaraghi[1], Adwait A. Trikanad[2], David Restrepo[2,3], Wei Huang[1] Steven Herrera[1], Jesus Rivera[1], Mikhail Zhernenkov[4] , Dilworth Y. Parkinson[5], Roy L. Caldwell[6], Pablo D. Zavattieri[2], David Kisailus[1,7]*

*Corresponding Author
Materials Science and Engineering Program
Department of Chemical & Environmental Engineering
MSE Building Room 343
University of California, Riverside
Riverside, CA 92521
david@engr.ucr.edu
Phone: 951-827-4310
Fax: 951-827-5696

[1]Materials Science & Engineering Program, University of California, Riverside, Riverside, CA 92521, USA
[2]Lyles School of Civil Engineering, Purdue University, West Lafayette, IN 47907, USA
[3]Department of Mechanical Engineering, The University of Texas at San Antonio, San Antonio, TX 78249, USA
[4] National Synchrotron Light Source-II, Brookhaven National Laboratory, Upton, NY 11973
[5] Advanced Light Source, Lawrence Berkeley National Laboratory, Berkeley, CA, 94720
[6]Department of Integrated Biology, University of California, Berkeley, Berkeley, CA 94720, USA
[7]Department of Chemical & Environmental Engineering, University of California, Riverside, Riverside, CA, 92521, USA

Mantis shrimp are aggressive marine crustaceans well known for their rapid and powerful hunting strategies, deploying highly specialized raptorial appendages to strike and kill prey with tremendous force and speed. Less well-known, however, is the ability of some species of mantis shrimp to defend themselves from the repeated blows of conspecifics during ritualized fighting using a shield-like segment of abdominal armor called the telson. Here, we examine multi-scale

structure-mechanical property relationships of this damage-tolerant biological composite in order to understand potential strategies that nature uses for resisting failure from repeated high-energy impacts. The telson structures of the smashing-type species, *Odontodactylus scyllarus*, and the less aggressive spearing-type species, *Lysiosquillina maculata*, are also compared in order to better understand the ecological pressures driving the formation and use of the telson as a biological shield. We identify a higher bulk compressive stiffness within the smasher telson, which is attributed to its concave macro-morphology, thicker cuticle, and higher degree of mineralization within its exocuticle. At the same time, the presence of ridges at the dorsal surface suggest a role in imparting compliance for energy absorption. Fracture analysis identifies an enhanced toughening mechanism of crack twisting within the smasher telson, attributed to its well-defined pitch-graded helicoidal fibrous micro-architecture. Such findings may prove useful for the design of lightweight graded composites materials with potential flexibility, multifunctionality as well as improved damage-tolerance.

1. Introduction

Many animals in nature rely on exoskeletal or dermal structures that are stiff and tough for protection against predators.[1] In some organisms, these structures also function as tools employed during ritualized combat and territorial disputes with conspecifics.[2] One such set of organisms is the stomatopods, more colloquially referred to as mantis shrimp, a group of marine crustaceans well known for their complex vision system, agnostic behavior, and powerful hunting strategies.[3] Stomatopods employ a highly developed set of raptorial appendages called dactyls for hunting and defensive purposes. Such appendages are commonly divided into two types: smashing and spearing. Species of the smashing type (smashers), which come from the Gonodactylidae family,

employ heavily mineralized bulbous club-like appendages (dactyls) to smash through the mechanically tough exteriors of their prey, which include mollusks, crabs, and other shelled organisms with tremendous force and speed.[3d, 3e] The smashing dactyl hereto referred to as the dactyl club can deliver impacts reaching speeds of 23 m/s and peak forces up to 1500 N.[3d] Conversely, the spearing variety (spearers), which comprise the Squillidae, Lysiosquillidae, Bathysquillidae, and some species of the Gonodactylidae families, employ slender dactyl structures containing several to many sharp spines and are used primarily for rapidly piercing and capturing soft-bodied prey such as fish.

In conjunction with the dactyl club, an offensive weapon, stomatopods possess a shield-like terminal segment of abdominal armor called the telson, which can also be used for personal protection during ritualized fighting and specifically grappling with conspecifics.[2b, 2g, 3b, 3d, 4] The telson structure is common amongst crustaceans and its primary function is to assist in the cardioid escape reaction, whereby rapid abdominal contractions create powerful swimming strokes that thrust the animal backwards to escape predators and other threats.[5] The telson, which is combined with the uropods to create the tail fin, contains a high surface area that acts as a paddle for rapid swimming. In the mantis shrimp though, specifically the smashers, the telson takes on more complex agnostic roles. Smasher stomatopods partake in an act called coiling, whereby they curl up and use their telson as a shield to either physically block the entrance to their dwelling place or absorb the directed impacts from the dactyls of conspecifics during one-on-one combat.[2b, 2g, 3a, 3b] The telson can endure repeated direct blows from the dactyl clubs of conspecifics without catastrophically failing, which suggests a similarly impressive and robust design. Additionally, observations made by Caldwell seem to suggest that the coiling behavior (i.e., using the telson to withstand directed dactyl strikes) is limited to the smashing type stomatopods.[3b] It has also been

noted that the most cavity-limited species of smashers are not only the most aggressive, but also possess the most heavily armored telson structures.[3b]

Smasher stomatopods, members of the Gonodactylidae family, commonly and historically dwell in pre-existing cavities in rock, rubble and coral, whereas spearers construct and inhabit burrows in substrates of sand or mud. Due to the limited availability and competition for cavity dwelling places, it is believed that smashers evolved more complex and intense agnostic behavior in comparison to spearers, which have access to an abundance of substrates and can thus relocate and rebuild their burrows, if necessary.[3b] Thus, it is expected that the telson structures have co-evolved with the intensity of agnostic behavior and damage potential of the raptorial appendage, resulting in smashers possessing more robust and damage-tolerant telsons.

Taylor and Patek examined the mechanical impact properties of the telson from the smashing species, *Neogonodactylus wennerae.*[2g] Measurements of the coefficient of restitution revealed an inelastic response of the telson structure, thereby allowing it to effectively absorb and dissipate 69% of the impact energy.[2g] Through micro-CT measurements, varying degrees of mineralization as well as morphological features including ridge-like regions called carinae were identified within the telson structure, which were hypothesized to impart a combination of stiffness and compliance necessary for energy absorption.[2g] Details, however, regarding the ultrastructural features, chemical composition, mechanical properties, and mechanisms underlying the telson's resistance to high-energy impact loading have not yet been uncovered. Recently, Zhang et al. identified a fibrous twisted plywood (helicoidal, Bouligand) microstructure, characteristic of most crustacean cuticles, within the telson of the smashing type mantis shrimp, *Odontodactylus scyllarus.*[6] Synchrotron x-ray micro-diffraction was also used to map the three-dimensional alpha-chitin fiber orientation, which revealed texturing corresponding to the helicoidal fiber

architecture.[6] A herringbone-like helicoidal microstructure was also recently identified within the offensive dactyl weapon of *O. scyllarus*, which contrasts the flat Bouligand design found within the defensive telson structure.[7]

In the present work, we seek to uncover and compare the multiscale structure-mechanical property relationships of the smasher and spearer stomatopod telsons from *Odontodactylus scyllarus* (peacock mantis shrimp) and *Lysiosquillina maculata* (zebra mantis shrimp), respectively. Such studies will not only reveal important clues as to the role of various ultrastructural features on imparting strength and toughness in biological composite materials, but they will also allow us to draw new conclusions as to role of selective pressures, namely habitat and agnostic behavior, on the evolution of impact-resistant biological armor in stomatopods.

2. Results

2.1 Macro-morphological features

Bulk specimens, as well as polished cross-sections, were initially examined by optical microscopy (**Figure 1**) to provide an overview of the macrostructural features of the smasher and spearer telsons. Figures 1A and 1C show representative anterior views of the smasher (*O. scyllarus*) and spearer (*L. maculata*) stomatopods, respectively. Dashed regions highlight the raptorial appendage and telson. Optical microscopy of the dissected smasher and spearer dactyls (Figures 1B and 1D, respectively) highlight significant differences in morphology. We note the hammer-like and spear-like nature of the smasher and spearer dactyls, representative of their utility in smashing through hard-shelled prey and impaling and capturing soft-bodied prey, respectively. Dorsal views of the corresponding dissected telson structures are similarly shown in Figures 1E and 1G, respectively. The two telson structures are similar in overall size. Both have comparable widths (23.5 ± 3.3 mm

vs. 20.6 ± 3.3 mm for smasher and spearer, respectively); however, the smasher telson is slightly longer (26.9 ± 4.0 mm) than the spearer telson (20.2 ± 3.2 mm). Comparison of the aspect ratio (length/width) thus reveals a longer, more elongated smasher telson (1.14 ± 0.04) compared to a more square-shaped spearer telson (0.98 ± 0.02).
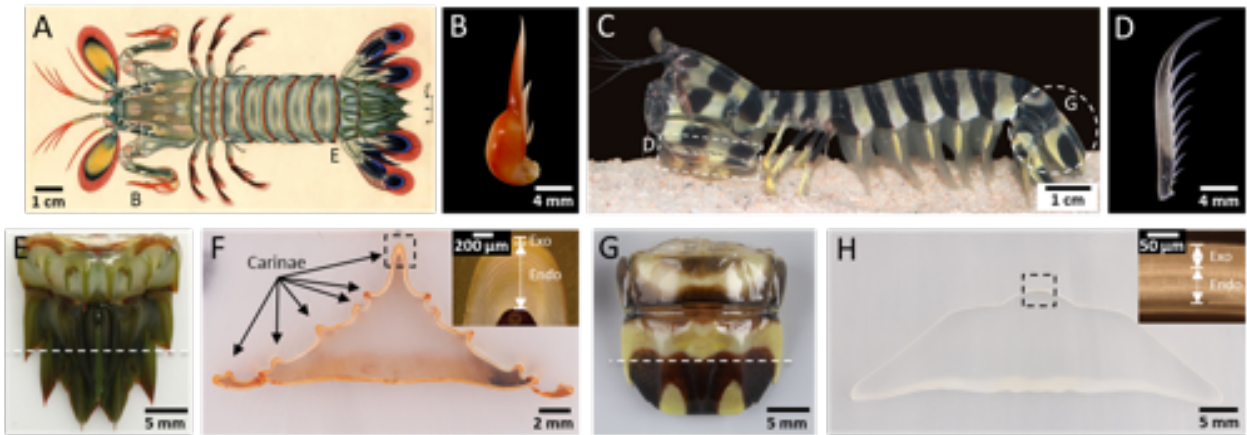

Figure 1. Telson overview & comparison of bulk morphologies. (A) *O. scyllarus* (smashing type stomatopod) highlighting the raptorial appendage and telson. (B) Hammer-like dactyl appendage of *O. scyllarus*. (C) *L. maculata* (spearing type stomatopod) highlighting the raptorial appendage and telson. (D) Spear-like dactyl appendage of *L. maculata*. (E) Telson segment of *O. scyllarus*. (F) Polished transverse cross-section of the smasher telson whose plane of section is denoted by the dashed line in (E). Inset showing higher magnification optical micrograph of dorsal cuticle along the medial ridge (dashed box). (G) Telson segment of *L. maculata*. (H) Polished transverse cross-section of the spearer telson whose plane of section is denoted by the dashed line in (G). Inset showing higher magnification optical micrograph of dorsal cuticle along center line (dashed box). Panel *A* adapted from Reference [8].

Noticeable differences in the telson bulk morphologies are also apparent. The smasher telson features many ridges on its dorsal surface. These ridges, called carinae, terminate into sharp

spines or teeth at the posterior edge teeth (Figure 1E). Conversely, the spearer telson has a fairly simple, smooth and rounded bulk morphology, lacking any well-defined carinae; although, some short and less-developed spines are apparent at the posterior edge (Figure 1G). Both smasher and spearer telsons can be used, in combination with spines found on the adjacent uropod structures, in an offensive effort to stab or push away conspecifics during agnostic interactions.[3b] However, the presence of more pronounced spines in the smasher telson reflects an evolutionary history of more intense agnostic interactions between the Gonodactylidae. Cross-sectional analysis of the smasher telson along the transverse plane (Figure 1F) reveals the highly contoured and concave morphology of the cuticle, with carinae lining the dorsal surface (denoted by black arrows). A unique feature of the telson from *O. scyllarus* is its pronounced (and largest) medial carina, which is located along the mid-plane. By comparison, the spearer telson cross-section (Figure 1H) shows a simple convex geometry, which lacks any high curvature regions along the dorsal surface due to the lack of carinae. A single broad (high radius of curvature) medial ridge is apparent in most spearer (*L. maculata*) telsons.

2.2 Microstructural features

Microstructural features of fractured and polished cross-sectional telson, from both smasher and spearer mantis, were subsequently examined by optical and scanning electron microscopy (SEM). Higher resolution optical micrographs of cross-sections along the mid-line of the dorsal cuticle (insets, Figures 1F and 1H, respectively) show a laminated appearance, which is characteristic of the helicoidal microstructure.[1f, 9] Measurements of regional cuticle thicknesses were taken for comparison. The thickest section for both smasher and spearer telsons was located at the medial dorsal region of the cuticle (approximately 700 μm and 100 μm, respectively). In general, the

smasher telson has a substantially thicker (approximately 2-7 times) cuticle than the spearer telson in any one region. While the spearer telson has a fairly uniform thickness (approximately 80-100 µm), the smasher telson is more varied. Ridged (carinae) regions are generally thicker than non-ridged areas of the cuticle, with the greatest thickness always along the medial carina (approximately 500-700 µm).

Fracture analysis of telsons along the sagittal plane (**Figure 2**), confirm that both structures consist of a helicoidal arrangement of alpha-chitin fibers. Low magnification SEM micrographs of the fractured smasher and spearer telsons along the medial dorsal cuticle (Figures 2A and 2D, respectively), reveal unidirectional alpha-chitin fiber sheets that are stacked and helicoidally rotated about an axis normal to the cuticle surface. Pore canal tubules, also composed of alpha-chitin fibers, interpenetrate the in-plane helicoidal fibers and are aligned normal to the cuticle surface (out-of-plane). These fiber-reinforced tubules not only serve as conduits for the transport of mineral species for resorption and deposition of mineral during periodic molting, but likely provide reinforcement against compressive and impact forces and enhanced toughness via crack deflection.[2f, 7, 9c, 10] Both smasher and spearer telson cuticles show finer stacking of fiber layers within the exocuticle (Figures 2B and 2E, respectively) compared to the endocuticle (Figures 2C and 2F, respectively), which is a common structural trait across the arthropod cuticle.[1f, 9a, 9e]
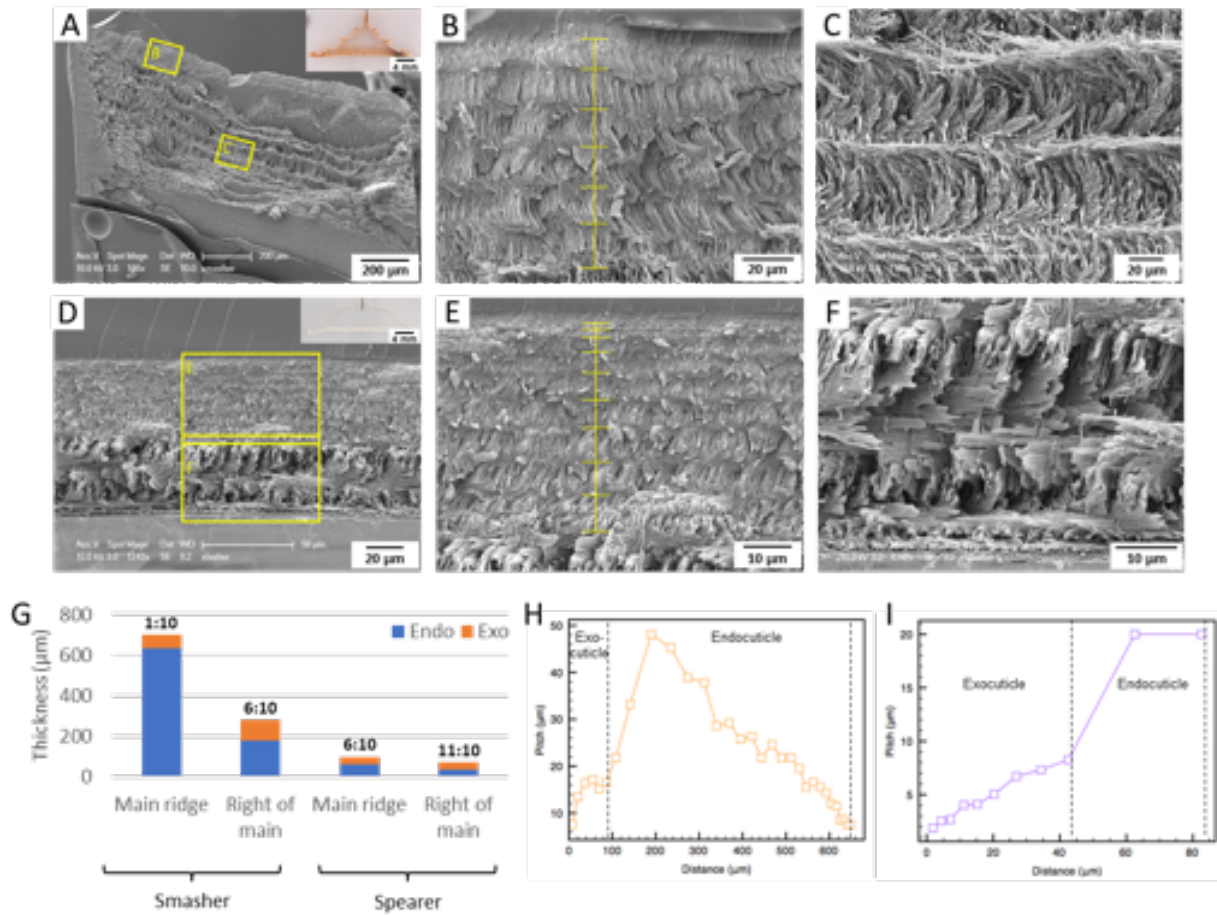
Figure 2. Microstructural features of the smasher and spearer telson. (A) Low magnification SEM micrograph of a fractured sagittal section of the smasher telson along the medial carina. Inset dashed line showing location of fracture. (B) Higher magnification SEM of the smasher telson exocuticle region denoted in (A) (yellow box). (C) Higher magnification SEM of the smasher telson endocuticle region as denoted in (A) (yellow box). (D) Low magnification SEM micrograph of the fractured sagittal section of the spearer telson along the center-line. Inset dashed line showing location of fracture. (E) Higher magnification of the spearer telson exocuticle region denoted in (D) (yellow box). (F) Higher magnification of the spearer telson endocuticle region as denoted in (D) (yellow box) showing pore canal fibers interspersed between rotating fibers. (G) Comparison of the local cuticle thicknesses along the telson center-line (medial carinae) and right of the center-line (non-ridged) for both the smasher and spearer telsons. Bar headers denote the ratio of exo- to endo-cuticle. (H) Plot showing gradient in the

pitch distance for periods of the helicoidal fibrous architecture along the medial carina within the smasher telson. (I) Plot showing gradient in pitch distance along the center-line of the spearer telson.

There are noticeable differences in the relative thicknesses of exo- and endo-cuticle regions from the smasher and spearer telsons (Figure 2G).The endocuticle represents 90% of the total cuticle thickness along the smasher medial carina, compared to 62% in the same region of the spearer telson. In non-ridged regions (i.e., right of the telson center-line), the relative thickness of endocuticle is significantly lower: 64% and 48% for the smasher and spearer, respectively. The higher overall thickness and relative fraction of endocuticle in ridged regions may suggest the role of ridges in providing higher localized stiffness as well as energy absorption through microcracking in instances where they serve as the first site of contact during an impact. In addition to the variations in the relative exo-/endo-cuticle thicknesses, we also note differences in the number of helicoidal periods and pitch length gradients amongst the smasher and spearer telsons. Line plots comparing the pitch length gradient through the exo- and endo-cuticle regions of the smasher and spearer telson (corresponding to the SEM micrographs in Figures 2A and 2D) are shown in Figures 2H and 2I, respectively. In one set of representative samples, the smasher telson features six periods of rotation within the exocuticle, with a pitch length increasing from the cuticle surface (i.e., dorsal) from approximately 7 μm to approximately 18 μm at the exo-/endo-cuticular interface. The pitch length continues to increase within the endocuticle, reaching a maximum pitch distance of nearly 50 μm before gradually decreasing to approximately 5 μm. These gradations occur over a total of 25 periods exist within the endocuticle, highlighting the presence of a smooth pitch gradient. By comparison, the spearer telson features a similar exocuticle with 9 periods of rotation and a pitch length increasing from approximately 2 μm at the cuticle surface to about 8

μm at the exo-/endo-cuticular interface. However, the spearer telson endocuticle only features two periods within the endocuticle, both of which have a pitch distance of approximately 20 μm, demonstrating the lack of a well-defined pitch gradient. Although the smasher telson has fewer periods of rotating fibers within the exocuticle than the spearer telson, it features a more highly developed endocuticle, which may contribute additional energy absorption during impact as well as localized stiffening to resist deformation upon impact.

2.3 Ultrastructural analyses

Dorsal views of the reconstructed μ-CT scans of the smasher and spearer telson (**Figures 3A**, 3B, top) show a higher overall x-ray attenuation within the smasher telson.
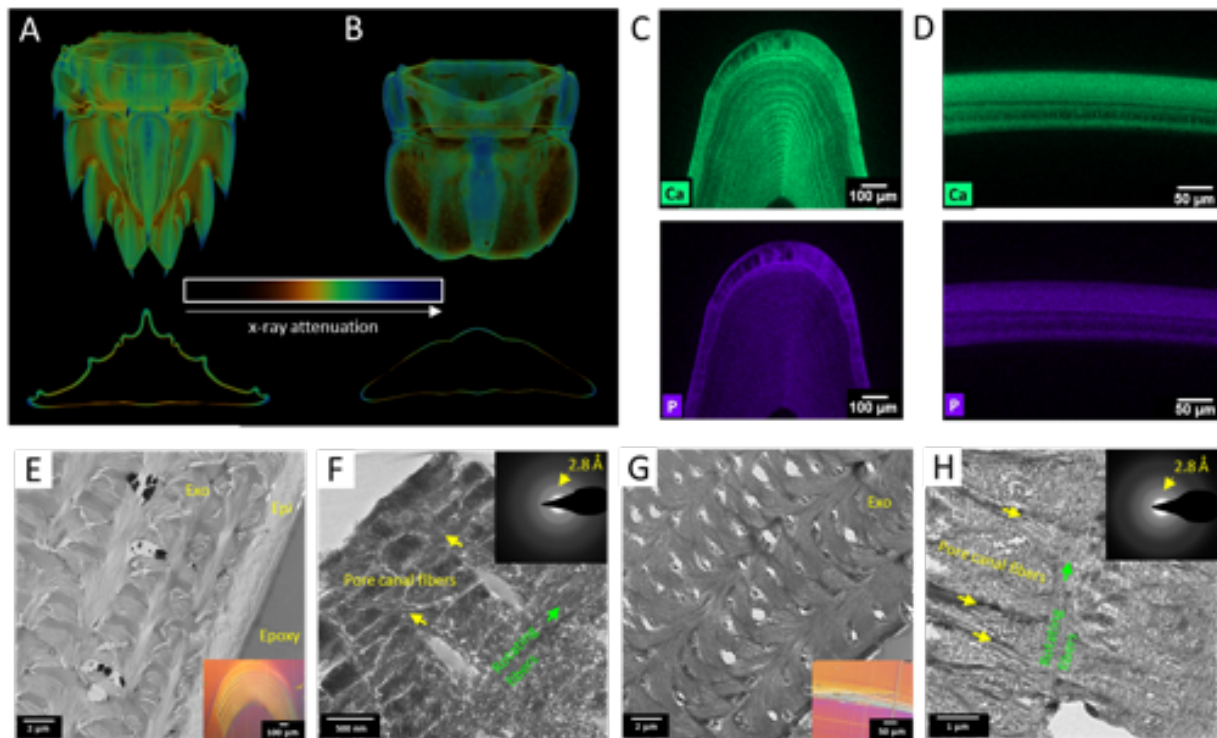

Figure 3. Mineralization gradients via micro-CT and TEM. (A) Micro-computed tomography reconstruction of the smasher telson dorsal view (top) and transverse cross-section (bottom). (B) Micro-computed tomography reconstruction of the spearer telson dorsal view (top) and transverse cross-section

(bottom). (C) Energy dispersive spectroscopy (EDS) maps showing local concentrations of calcium (green, top) and phosphorus (purple, bottom) within the smasher telson medial carina. (D) EDS maps showing local concentrations of calcium (green, top) and phosphorus (purple, bottom) along the spearer telson centerline. (E) Bright-field TEM of the smasher exocuticle near the telson surface. Inset showing optical micrograph of microtomed area, which is along the medial carina. (F) High magnification within the smasher telson exocuticle showing pore canal tubule and rotating fibers. Inset diffraction pattern showing nanocrystalline mineral. (G) Bright-field TEM within the spearer telson exocuticle. Inset showing optical micrograph of microtomed area, which is along the center-line. (H) High magnification within the spearer telson exocuticle showing pore canal tubule and rotating fibers. Inset diffraction pattern showing diffuse rings signifying weakly crystalline mineral.

The highest x-ray attenuation for both telson specimens occurs along the mid-plane of the long axis (along the medial carina in the smasher telson and centerline of the spearer telson), suggesting greatest structural reinforcement in the area where impact is most likely to occur. The spines or teeth of the smasher telson also appear to be heavily mineralized. Cross-sectional analysis clearly shows a thinner spearer telson cuticle as compared to the smasher telson (Figure 3A, 3B, bottom). The dorsal cuticle of the smasher telson also appears to be thicker and/or more heavily mineralized than the ventral cuticle.

EDS mapping along the mid-plane of the smasher and spearer telsons (Figures 3C and 3D, respectively) confirms that the exocuticular region of both structures are more heavily mineralized than the endocuticular regions, containing higher concentrations of calcium and phosphorus. While the trend is consistent for both telson structures, the difference appears to be more substantial for the smasher telson. The higher degree of mineralization within the exocuticle relative to the endocuticle as compared to that in the spearer telson may suggest the need for a stiffer outer impact

region to provide additional resistance to deformation and/or puncture-resistance from impact. The presence of magnesium in both telsons also suggests its role in stabilizing the amorphous or nanocrystalline mineral.[11]

Bright field TEM of microtomed thin (<100 nm) sections of smasher and spearer exocuticle regions along the mid-plane (Figures 3E, 3G) reveals the nested arc laminated pattern, characteristic of the helicoidal architecture of fibers. High magnification imaging reveals that the mineralized alpha-chitin fibers are approximately 44.4 ± 5.7 nm in diameter. We can observe and distinguish the fibers that make up the interpenetrating pore canal tubules, which are oriented normal to the telson surface, from the rotating fibers (Figures 3F, 3H). Selected area electron diffraction within the exocuticle regions of the smasher and spearer telsons reveals diffuse rings, indicative of poorly ordered mineral phase (insets, Figures 3F, 3H). The most intense yet still diffuse diffraction ring, corresponding to a d-spacing of approximately 2.8 Å, matches closely with that of apatite (121) and (211) reflections and indicates that the mineral phase consists of randomly oriented nanocrystals.[12] The presence of high concentrations of phosphorus from EDS analysis suggests that the mineral is likely carbonated apatite as opposed to a phosphate-substituted calcium carbonate phase. Similar mineral phases have been identified within the dactyl club of *O. scyllarus*.[7, 13] In addition, x-ray diffraction analysis of ground specimens of smasher and spearer telson reveal broad peaks, suggesting the presence of amorphous or weakly crystalline mineral phases (See Figure S1A, Supporting Information). A prominent x-ray diffraction peak (d = 4.43 Å, α-chitin (110)) also confirms the high abundance of α-chitin within each cuticle structure.[12, 14] The slightly more diffuse electron diffraction ring (larger full width at half-maximum intensity) at 2.8 Å observed in the spearer telson lamellae (inset, Figure 3H) as compared to that of the smasher telson lamellae (inset, Figure 3F) suggest less ordering of mineral in the spearer telson.

Thermogravimetric analysis/differential scanning calorimetry of powdered smasher and spearer telsons reveal similar compositions, each containing approximately 55-60 wt% mineral, 30 wt% organic matter, and 10-15 wt% water (See Figure S2, Supporting Information). Similar amorphous mineral and organic contents, yet drastically different bulk compressive properties seem to suggest that the micro- and macro-structures of the telsons dominate their mechanical behavior.

2.4 Nano-mechanical properties

To compare the regional mechanical properties of the telson structures, nanoindentation mapping was performed on polished cross-sections. **Figure 4** shows the results of indentation maps along the second lateral carina and center-line of the smasher and spearer telsons, respectively. Both smasher and spearer telsons show gradients in reduced elastic modulus and hardness across the exo-/ endo-cuticular interface, which are consistent with the elemental trends from EDS mapping. The reduced elastic modulus and hardness are highest within the exocuticle (approximately 6-8 GPa and 0.3-0.45 GPa, respectively for the smasher telson, Figure 4C), whereas modulus and hardness values within the endocuticle are approximately 2 GPa and 0.1 GPa, respectively. Nanomechanical properties within the spearer telson (Figure 4D) are similar to those of the smasher telson, with a broader variation of elastic modulus. Reduced elastic modulus and hardness range from approximately 2-14 GPa and 0.1-0.5 GPa, respectively. The change in mechanical properties, however, between the exo- and endo-cuticle regions of the spearer telson is less apparent. While the reduced modulus map shows a decreasing trend in modulus from the exocuticle to the endocuticle, no apparent gradient is observed within the hardness map. This contrasts with the smasher telson, which shows a sharp decrease in elastic modulus and hardness transitioning from the exocuticle to the endocuticle region. This may be correlated with

compositional changes in the mineral (as observed in the EDS maps, which show a more pronounced gradient in concentration of calcium and phosphorus across the exo- and endo-cuticle regions in the smasher telson than in the spearer telson).
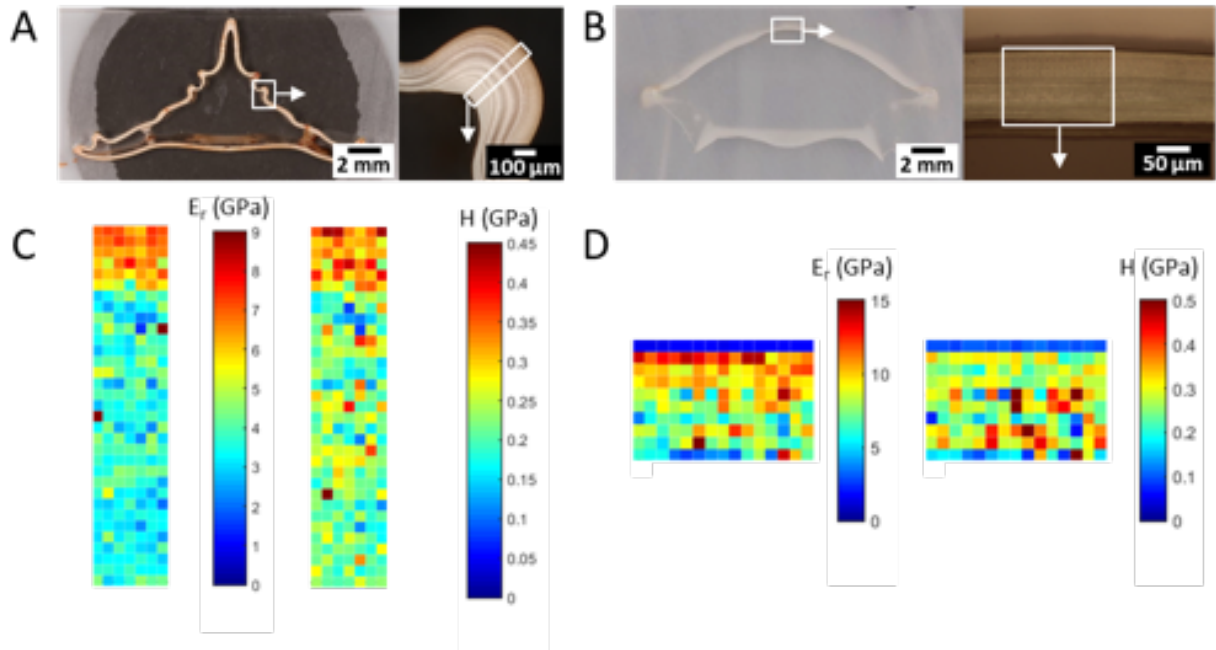

Figure 4. Nanoindentation mapping of telson cross-sections. (A) Optical micrographs of the smasher telson transverse cross-section (left) and second lateral carina (right). (B) Optical micrographs of the spearer telson transverse cross-section (left) and center dorsal cuticle (right). (C) Nanoindentation maps of reduced elastic modulus (left) and hardness (right) within the second lateral carina of the smasher telson (area denoted by the boxed region from (A). (D) Nanoindentation maps of reduced elastic modulus (left) and hardness (right) within center-line dorsal cuticle of the spearer telson (top) (area denoted by the boxed region from top).

Although the μ-CT seems to suggest that the medial regions of the telsons are more heavily mineralized, nanoindentation mapping in various regions (e.g., lateral carinae and lateral non-carinae areas of the smasher telson, lateral areas of the spearer telson) shows similar ranges of

reduced elastic modulus and hardness. This suggests that the increased x-ray attenuation along the telson mid-plane is due to higher cuticle thickness, not necessarily higher relative mineral content per cuticle thickness. Examples of structures in nature varying their thickness as opposed to adding mineral to enhance mechanical performance are numerous. For instance, a thicker cuticle in some species leads to higher safety factors in the claws of *Cancer* crabs, egg shells with higher shell thickness report higher breaking strengths, and cortical thickness plays a major role in determining bone strength.[15]

2.5 Bulk mechanical testing of telsons and 3D printed mimics

Quasi-static compression testing was performed to assess and compare the strength and stiffness of the bulk smasher and spearer telsons. Hydrated and dried telson specimens were loaded in a parallel plate configuration and compressed cyclically to a controlled displacement of 500 μm at a rate of 10 μm/s. Telson samples were also cut, using a razor blade, along the flexible soft tissue separating the two segments of the bifurcated telson, which we call here the anterior and posterior telson segments. This was done to also compare their load bearing capabilities in order to assess if either segment plays a larger role in the overall stiffness response of the structure. **Figure 5A** shows images of the dissected anterior and posterior segments of the smasher and spearer telsons.
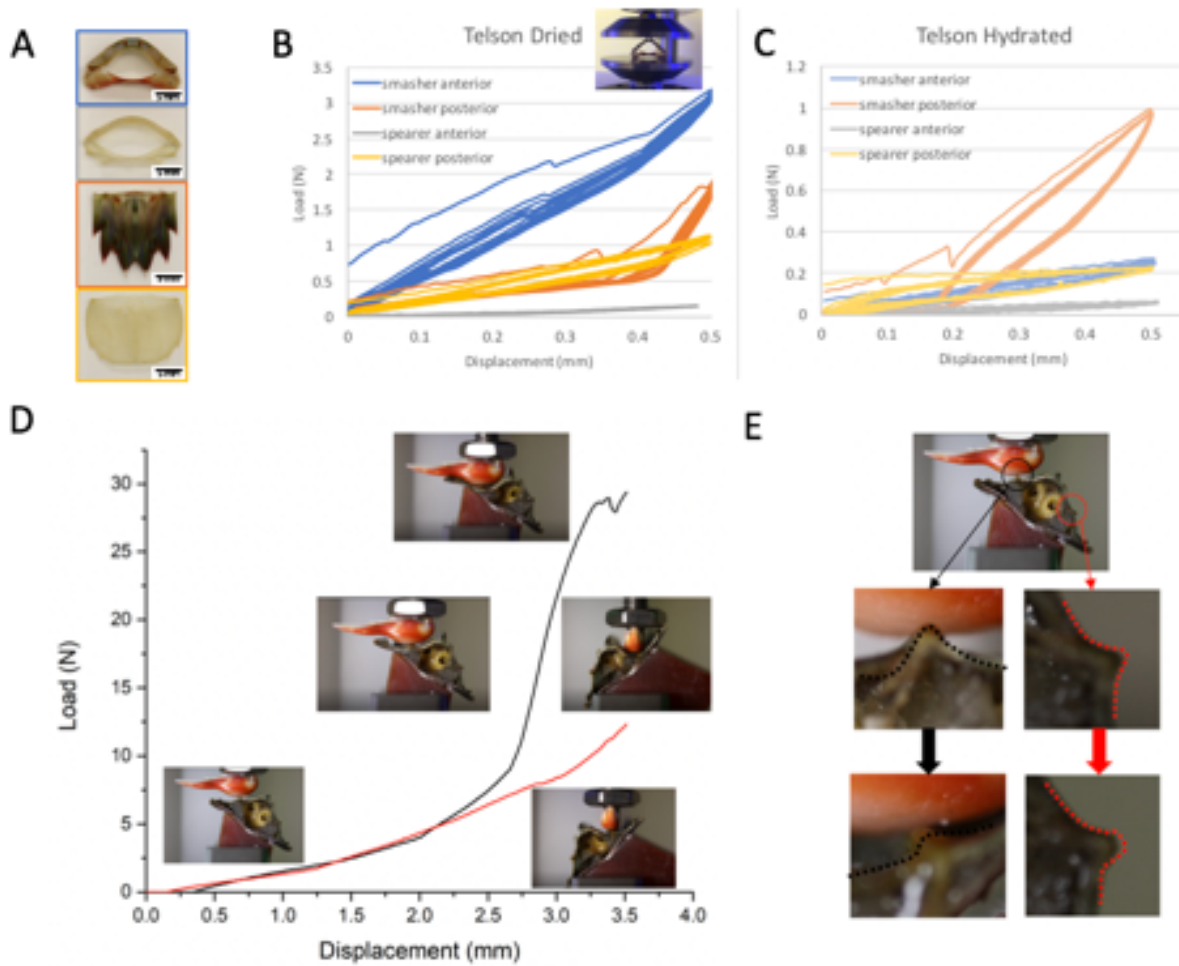
Figure 5. Compression testing of natural and biomimetic telson structures. (A) Images of the dissected anterior and posterior segments of smasher and spearer telson (from top to bottom: anterior smasher, anterior spearer, posterior smasher, posterior spearer). (B, C) Load-displacement plots showing results of cyclical compression tests on the smasher and spearer anterior and posterior telson segments under dried (B) and hydrated (C) conditions. (D) Load-displacement curves showing results of compression testing on biomimetic 3D printed telson geometries. Insets show images of the triangle control (top), concave (middle), and convex (bottom) 3D printed transverse cross-sectional geometries before testing (left) and at peak load (right). Notice the buckling of the triangular and convex parts. (E) Bar graph showing average compressive stiffness of the triangle, smasher, and spearer mimetic parts.

Load-displacement results for compression testing of the smasher and spearer telson segments under dried and hydrated conditions are shown in Figure 5B and 5C, respectively. Comparison of the compressive stiffness, measured by the slope of the load-displacement curve, shows that the smasher telson has a substantially higher stiffness than that of the spearer for both anterior and posterior segments under both dried and hydrated conditions. All dried samples show higher stiffness than hydrated samples, as expected. Hydrated biological tissues typically have higher extensibility and lower stiffness as compared to the dry state, due to water's ability to act as a plasticizer by forming hydrogen bonds between the polymer chains of organic fibers. The anterior smasher sample showed the greatest change in stiffness between dried and hydrated states. This could perhaps be attributed to a higher content of organic material within the anterior smasher than other samples, which may become very stiff when dried.

In addition, posterior segments show higher stiffness than anterior segments within each smasher and spearer telson. This makes intuitive sense since the posterior segments make up most the telson volume and are thus likely to bear the primary loads from attacks from predators and conspecifics. Comparing posterior telson segments, the smasher showed bulk compressive stiffnesses of 14.88 N/mm and 2.69 N/mm under dried and hydrated conditions, respectively, while the spearer telson reported stiffnesses of 0.94 N/mm and 0.36 N/mm, respectively. The stiffnesses of the anterior segments were 5.51 N/mm and 0.45 N/mm for the smasher telson under dried and hydrated conditions, respectively, and 0.29 N/mm and 0.11 N/mm for the spearer, respectively.

Quasi-static compression tests (strain rate $\sim10^{-3}$ s^{-1}) on the side of a freshly prepared and hydrated telson were conducted using a dactyl club as the compression loading head to mimic the natural loading scenarios (Figures 5D and E). Lateral expansion and flattening of carinae (Figure 5E, black dashed line) were observed when loading was applied to the side of the telson, enabling

energy dissipation by the large deformation of soft tissue within the structure. While on the other side of the telson, the curvature of the carinae become sharper (Figure 5E, red dashed line) due to the compression forces on this side. Interestingly, the deformation on the telson are recoverable during the loading and unloading tests. Thus, the carinae structure on the sides of the telson are acting as elastic "springs", providing lateral space for deformation.

Compression testing of 3D printed mimetic telson cross-sections was subsequently performed to assess the role of macro-morphological features of the telson, such as carinae and overall curvature, on the bulk mechanical properties. As we recall from the cross-sectional geometries of the smasher and spearer telsons (Figures 1F, 1H), the smasher telson features a concave dorsal cuticle, compared to the spearer telson, which features more of a convex geometry. To understand the effect of this curvature on mechanical performance, simplified truss structures were first modeled and then 3D printed. Concave and convex parts, featuring the same radius of curvature of the smasher and spearer telson dorsal cuticles, respectively, as well as a triangular truss structure, used as a control, were modeled, printed, and then compressed. The load-displacement curves for the smasher and spearer telson mimics as well as the triangular control are shown in Figure S3, Supporting Information. Comparison of the load-displacement data shows that the smasher (concave) telson cross-sectional geometry produces a substantially higher bulk compressive stiffness compared to concave geometry of the spearer telson mimic: 361.51 ± 73.52 N/mm versus 68.85 ± 6.72 N/mm, respectively. The concave geometry also reaches a peak compressive load (317.46 ± 22.34 N) that is more than six times higher that of the convex geometry (51.40 ± 4.60 N). Based on this observation, it is expected that the higher compressive stiffness and load-bearing ability of the natural smasher telson structure can be attributed in part to its concave macro-morphology as compared to the spearer's convex curvature. This is an important

design cue that can provide insight to nature's ability impart structural stiffening by varying the macro-morphology of its structures.

2.6 Finite element analysis on effect of ridge geometry

To assess the effect of the carinae geometry on the compressive stiffness of the telson, finite element simulations were performed on five different 3D models (**Figure 6A**). CAD models for the smasher (denoted as SMSH) and spearer (denoted as SPER) telsons were derived from micro-CT scans. To isolate the effect of the lateral ridges and medial carina, three additional models were created based on the smasher telson through CAD manipulation. One geometry retained the lateral ridges but removed the medial carina (denoted as NCCR). In another modified model, the lateral ridges were removed, while the medial carina was preserved (denoted as NRCC). The final modified model consisted of a smoothened version of the smasher telson (i.e., no medial carina and no lateral ridges, while maintaining the macro-curvature of the smasher telson; denoted as SMTH). Simulations were performed under two loading conditions; compression between two plates and a lateral loading event against a sphere with a curvature similar to a dactyl club. To further probe the effects of the ridge geometry, two more data sets were compiled. K1 SMTH refers to a variant of the smooth model (SMTH) for which the stiffness of the SMTH model was analytically scaled with a scaling factor K1, to match the stiffness of the smasher (SMSH) under top loading. Then this same scaling factor K1 is used on the SMTH data set to determine the stiffness response of K1 SMTH under lateral loading. Similarly, K2 SMTH is a scaled version of the SMTH stiffness to match that of the SMSH under lateral loading using a scaling factor K2. The scaling factor K2 is then used on the SMTH data set to obtain the stiffness response of K2 SMTH under top loading. Mean stiffness within error bounds was calculated for all models for up

to 0.5 mm displacement under top loading (Figure 6B) and lateral loading (Figure 6C). The percentage change in stiffness as compared to the smasher (SMSH) model was calculated for top loading (Figure 6D) and lateral loading (Figure 6E) using the equation:

$$\%change = \frac{K_{model} - K_{SMSH}}{K_{SMSH}} * 100$$

Here, K_{model} is the stiffness for each respective model and K_{SMSH} refers to the stiffness of the smasher telson. Comparison of the stiffness data shows that the loading direction plays a significant role on the effects of the carinae on stiffness response. Under top loading, the models containing the medial carina (SMSH and NRCC) show high stiffness as compared to the models that do not have the medial carinae (NCCR and SMTH). At the same time, the lateral ridges seem to add some compliance to the system (SMSH vs NRCC). The models without the medial carina show very low stiffness, as does the spearer model. Under lateral loading, the effect of the medial carina was noticeably reduced, though it still provided some stiffness to the system. Conversely, the effect of the lateral ridges providing compliance seemed to be enhanced (SMSH vs NRCC or SMTH vs NCCR). The spearer model continued to show low stiffness in comparison, which can be attributed to the differences in macro-curvatures between the smasher and spearer geometries. K1 SMTH and K2 SMTH are useful tools in showing the effects of scaling (achievable through modifications of thickness or Young's Modulus) on stiffness under multiple loading directions. K1 SMTH which matches the stiffness of the SMTH model to that of the SMSH model under top loading, showed a disproportionately large response under lateral loading, with stiffness values of several orders of magnitude above that of the SMSH model. K2 SMTH which matches the stiffness of the SMSH model under lateral loading, showed an almost negligible change in stiffness as compared to SMSH under top loading. These two data sets provide valuable insights in the importance of evolving these ridged geometries as opposed to simple changes in thickness. These

results highlight the subtle interplay between the stiffness provided by the medial carinae and the compliance provided by the lateral carinae to give the smasher telson its stiffness response under multiple directions of loading. They provide useful design cues, in manipulating the stiffness of structures under multidirectional loading.
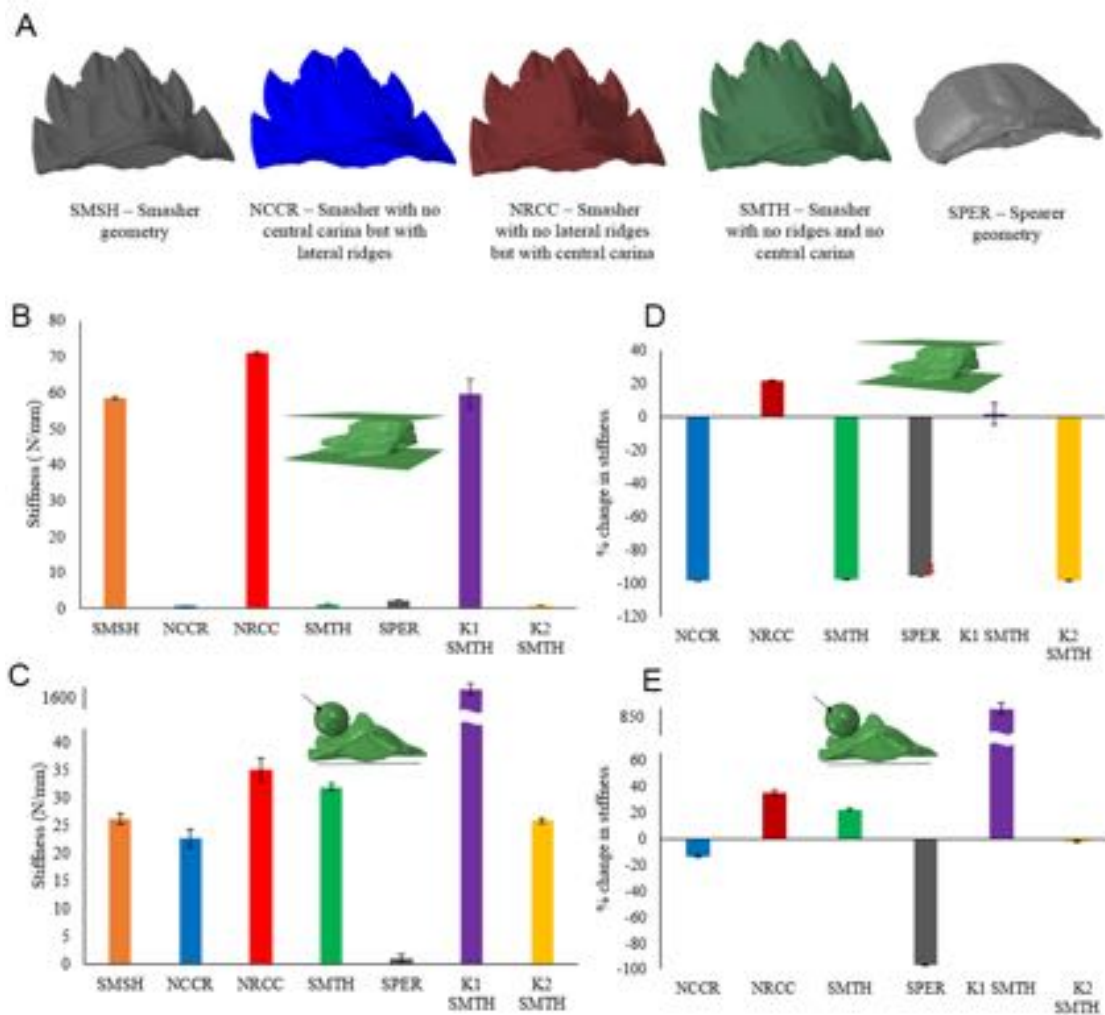

Figure 6. FE simulations on the effect of the carinae geometries on stiffness. (A) Representations of CAD models used in the FE simulations with nomenclature. (B) Mean stiffness for top loading up to 0.5 mm displacement (inset: loading scenario). (C) Mean stiffness for lateral loading up to 0.5 mm displacement (inset: loading scenario). (D) Percentage change in stiffness (as compared to the smasher model) under top loading. Corresponding change in stiffness for the spearer geometry obtained from experimental data under

top loading has been highlighted. (E) Percentage change in stiffness (as compared to the smasher model) under lateral loading.

2.7 Micro- and nano-scale toughening mechanisms of the telson cuticle

Characterization of failure processes in materials is critical for understanding and identifying potential mechanisms to resist fracture. Ex-situ compressive loading was thus performed on polished smasher and spearer telson cross-sections to observe crack propagation and identify toughening mechanisms. **Figures 7A-D** show backscattered electron (BSE) micrographs of a smasher telson cross-section loaded in compression to approximately 10% strain. Highly tortuous cracking is observed along the lateral side of the medial carina (Figure 7A). The inset shows a low magnification BSE micrograph of the cross-section loaded in a compression apparatus. A higher magnification micrograph within the cracked area (Figure 7B) reveals a sinusoidal crack path, which is indicative of a crack twisting failure mode characteristic of the helicoidal fibrous architecture found within the cuticle.[13, 16] By having a rotating crack front, the propagating crack is forced to twist, guided through the amorphous mineral by the architectural arrangement of fibers, which significantly enhances the work of fracture.[7, 13, 16-17] Microcracks branching off the main twisting crack front are also observed, which also improve the toughness of the material by reducing the crack tip stress concentration.[10c, 18] Fracture is also observed along the valley region between the left first and second lateral carinae (Figure 7C). The cracking pattern is also indicative of a crack twisting failure mechanism. Figure 7D reveals that toughening also exists in the form of crack twisting within the densely packed, more heavily mineralized exocuticle region of the smasher telson. The amorphous and mechanically isotropic nature of the mineral may be important

for enabling cracks to propagate along the organic fibers, thus allowing the helicoidal fiber architecture to facilitate a twisting crack pattern.
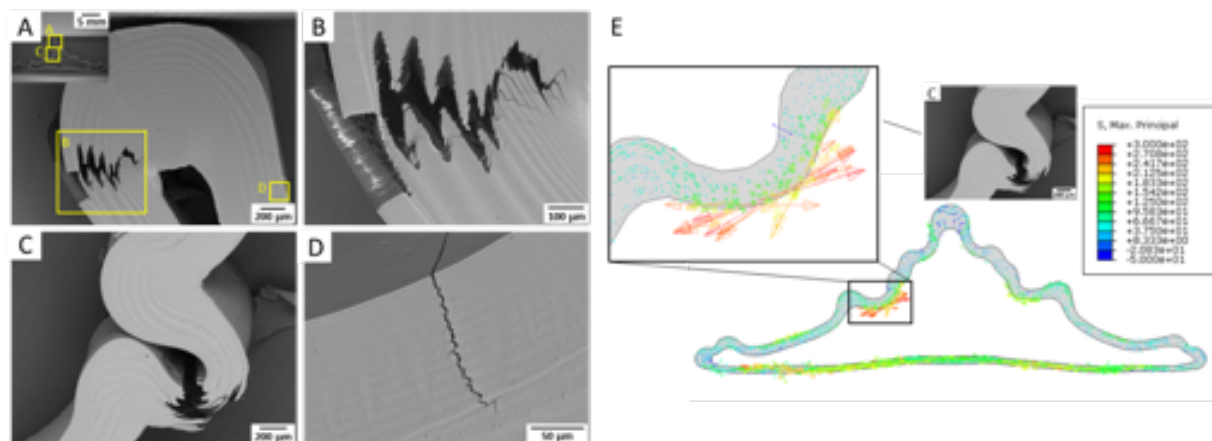

Figure 7. Ex-situ compression testing of smasher telson cross-section. (A) Low magnification backscattered electron (BSE) micrograph showing fracture along the lateral side of the medial carina of the smasher telson. Inset shows low magnification BSE micrograph of the overall telson cross-section loaded in the compression vice to 10% strain. (B) Higher magnification of the fractured cuticle from (A) showing sinusoidally twisting cracks within the exo- and endocuticle regions. Microcracks are also observed emanating from the crack front. (C) Catastrophic fracture between the first and second left lateral carina of the smasher telson. A twisted fracture path is also observed. (D) High magnification BSE micrograph within the exocuticle showing a nested arc crack pattern. (E) Principal stress directions in the smasher telson under top compressive loading, which highlights the stress concentration and match between principal stress directions and fracture zones observed in (C).

By comparison, the spearer telson cross-section was loaded to 20% strain and minimal controlled fracture was observed (See Figure S4, Supporting Information). Examination along the center-line of the dorsal cuticle (Figure S4 A) showed minimal cracking with some delamination within the endocuticle. The inset figure shows a low magnification BSE micrograph of the spearer telson cross-section loaded to 20% strain in the compression apparatus. In one lateral area of the

dorsal cuticle, fracture was observed (Figure S4 B) and is characterized by a fairly non-tortuous crack normal to the cuticle surface through the exocuticle followed by a longitudinal crack traversing the endocuticle. Little evidence of any crack twisting failure mechanisms is apparent in the spearer telson. Other lateral regions of the dorsal cuticle (Figures S4 C, D) show similar delamination within the endocuticle without any tortuous crack paths. Additional FE analysis of the principal stresses within the spearer telson cross-section subjected to uniaxial compression (data not shown here) suggests that the region of fracture shown in Figure S4 B undergoes predominantly bending stresses, which is consistent with the observed fracture pattern.

3. Discussion

In this work we characterized and compared the multi-length scale structures, composition and mechanical properties of the stomatopod telson from two temperamentally- and evolutionarily-different species: *O. scyllarus* and *L. maculata*, of the smashing-type and spearing-type variety. Structure-mechanical property relationships were derived to compare and better understand the material characteristics responsible for imparting enhanced damage-tolerance in the telson. The smasher telson revealed mechanical properties, such as bulk compressive stiffness and fracture-tolerance, far superior to those of the spearer telson. Bulk compressive testing of the telson segments showed substantially higher stiffness in the smasher telson. This enhancement is likely a result of a more sophisticated macro-morphology, namely the higher overall cuticle thickness and a concave geometry. Conversely, the presence of ridge-like structures called carinae impart transverse compliance for energy absorption. This suggests that the evolution of a ridged dorsal surface (i.e., carinae) as well as concave morphology in the smasher telson was an advantageous

trait for its use as a defensive structure, requiring adequate stiffness to prevent puncture, yet sufficient compliance to absorb the impact energy.

Corrugation, resembling the ridged smasher telson dorsal surface, has been incorporated into many engineering structures (e.g., cardboard packaging, roofs and flooring, hoses and pipes), as a means of forming lightweight materials that are also mechanically anisotropic, possessing high stiffness transverse to the corrugation direction and compliance along the corrugation direction.[19] Corrugated structures are also advantageous in yielding good resistance to buckling, as well as providing energy absorption from impact and resistance to shear and compressive loads.[19a] Questions though remain as to the multifunctional role of the smasher and spearer telson macro-morphologies, such as hydrodynamic drag for improved locomotion or even advantages for digging burrows in muddy or sandy substrates amongst the spearing stomatopods. Such features may be important or necessary for functions aside from self-defense and protection against predators and conspecifics.

The variation amongst telson microstructures and gradients begs the question as to the role of local cuticle thickness, number of helicoidal layers, and pitch gradients on the local stiffness and energy absorptive properties of the cuticle. Clear differences in the fracture behavior of the smasher and spearer telson cuticles were observed, in which a highly tortuous sinusoidal crack pattern was revealed in the smasher telson (seemingly yielding higher toughness), yet the spearer telson showed relatively straight cracks. An obvious question arises as to why a tortuous crack pattern is observed within the smasher telson, but not in the spearer telson. One hypothesis is that the more developed endocuticle in the smasher telson, featuring more periods of rotation and a well-defined pitch gradient, may facilitate slower and more controlled crack propagation, allowing for crack deflection at fiber layer interfaces and ultimately a crack twisting mechanism. In fact,

previous work by Grunenfelder et al. investigating the effect of inter-ply rotation angle on the impact-resistant properties of biomimetic helicoidal composite laminates as well as mechanical modeling work by Suksangpanya et al. found that certain rotation angles may facilitate a crack twisting mode of failure as opposed to a non-deflected crack propagating across fiber layers.[16, 20] Guarin-Zapata et al. also found that certain pitch gradients in laminated helicoidal structures can effectively filter out shear waves from an impact event.[21] The lack of a well-defined pitch gradient as well as few helicoidal periods within the endocuticle in the spearer telson may explain why predominately delamination failure modes are observed instead of a highly tortuous crack path. A more developed endocuticle and more well-defined pitch gradient in the smasher telson may have evolved in response to more intense agnostic interactions and to prevent damage from dactyl strikes.

These structural features and resultant mechanical properties reflect the evolutionary history of the stomatopods and the necessity for more damage-tolerant defensive structures in the smashers. Limited availability of coral cavity dwelling places for the smashers led to more aggressive behavior and agnostic interactions amongst the smashers.[3b, 22] Smashers with more heavily fortified telsons were likely able to better defend their habitant, ensuring their reproductive success and the proliferation of mantis shrimp with heavily armored telsons. Conversely, an overtly damage-tolerant spearer telson was likely not as necessary. Since the availability of sandy/muddy substrates for dwelling was in high supply, the spearers likely never developed a highly aggressive behavior amongst conspecifics and thus may not have necessitated a defensive telson structure. Although, it is worth noting that spearers' aggressiveness appears to be strongly correlated with the sophistication of their burrows and energy put into the construction of their habitats.[22]

Nonetheless, there is still much that can still be learned from the diversity of the stomatopod telson. Numerous species have been identified that are highly cavity-restricted, barely ever leaving their homes. These mantis shrimp display heavily armored telsons and even sport defensive features such as long spines (*Echinosquilla guerinii*) that emanate radially from the dorsal surface, mimicking a sea urchin.[2b, 22-23] Additional research will be required to better understand the role of environmental pressures on the evolution of defensive structures not only within the stomatopods, but other biological organisms as well, with the hope that these insights may provide inspiration for the development of useful engineering tools and structures.

4. Conclusions

The results reported here detail the multi-scale structure-mechanical property relationships in the shield-like segments, telson, used by mantis shrimp to defend themselves. Ultrastructural and mechanical analyses of telson structures from the smashing-type species reveal a higher bulk compressive stiffness versus that of the spearing-type of mantis, which is attributed to its concave macro-morphology, thicker cuticle, and higher degree of mineralization within its exocuticle. A primary medial ridge in the smashing telson provides out of plane stiffness, whereas the presence of ridges called carinae, located at the dorsal surface, suggest a role in imparting compliance for energy absorption. Microstructural analyses uncover the presence of the Bouligand or helicoidal architecture, which has been identified to enhance toughening via crack twisting. These studies illustrate several design principles that could be potentially applied to the design of lightweight graded composites materials with potential flexibility, multifunctionality as well as improved damage-tolerance.

5. Experimental Section

Specimens: Smasher and spearer telson specimens were provided from live organisms of *Odontodactylus scyllarus* and *Lysiosquillina maculata*, respectively. Organisms were purchased from a commercial supplier and housed and maintained in an in-house sea-water system. Prior to testing, animals were placed in a refrigerator until dead and dissected thereafter. Molt cycles were carefully monitored and only animals in the inter-molt phase were selected for study. Measurements of bulk length and width were taken from optical images of eight smasher and six spearer telsons.

Optical and electron microscopy: For analysis of polished cross-sections of the telson structures, specimens were initially dehydrated in air at room temperature and then embedded in epoxy (System 2000, Fibre Glast Developments Corporation, USA) and cured at 60°C for 1 hour. Samples were subsequently sectioned along the desired orthogonal plane using a low speed diamond saw (TechCut 4, Allied High Tech Products Inc., USA) and polished using a manual grinder/polisher (MetPrep 3, Allied High Tech Products Inc., USA) with graded silicon carbide paper and diamond abrasive solutions down to 50 nm grit size. Polished samples were washed in DI water in between steps to prevent cross-contamination and finally washed and sonicated in DI water for 5 minutes to remove any abrasive material from the polished surface. For analysis of fractured sections of the telson, 1-2 mm thick sections of embedded telson were cut using the low speed diamond saw and mechanically fractured by bending along the desired plane. All samples were subsequently sputter coated with a thin layer of platinum and palladium for conductivity and imaged using a scanning electron microscope (XL-30-FEG, Philips, USA or MIRA3 GMU, TESCAN, USA) at 10 kV accelerating voltage. Transmission electron microscopy and selected area electron diffraction were conducted using a TEM (Tecnai12, FEI, USA) operated at 120 kV

accelerating voltage. Thin sections, approximately 70 nm thick, for TEM were prepared using an ultramicrotome (XT-X, RMC Boeckeler, USA).

Micro-computed tomography: Micro-CT scans of the smasher and spearer telson were acquired using an Xradia 510 Versa (Zeiss, Germany) operated at 70 kV. Reconstruction, volume rendering, and visualization were performed using Amira 3D (FEI, USA) and CTvox (Bruker, USA) software packages.

Energy dispersive spectroscopy: Standardless elemental mapping and analysis was conducted on non-coated polished cross-sections of the telson structures using a field-emission SEM (MIRA3 GMU, TESCAN, USA) operated at 20 kV and a Quantax 400 EDS system equipped with dual xFlash 6 SSD detectors (Bruker, USA). Elemental maps were collected for 10-15 minutes.

Nanoindentation: Nanoindentation mapping within the telson cross-sections was performed using a TI-950 TriboIndenter (Hysitron, USA). The spearer telson map featured a 15 by 10 point array with 10 μm spacing between indents. A trapezoidal (5 second load, 2 second hold, 5 second unload) quasi-static load function was used. Indents were made using a diamond cube corner probe and controlled in displacement to a peak depth of 1 μm. The smasher telson map consisted of a 33 by 7 point array with 10 μm spacing between indents. A similar trapezoidal (5 second load, 2 second hold, 5 second unload) quasi-static load function was used. Indents were made using a diamond cube corner probe and controlled in displacement to a peak depth of 500 nm.

Compression testing and 3D printing: Compression tests on bulk telson segments were performed using an ElectroForce 3200 Series III mechanical tester (Bose, USA). Telson structures were compressed between two steel parallel plate fixtures. A pre-load of 20 mN was applied to ensure contact before testing. Telson structures were compressed to 500 μm relative displacement at a rate of 10 μm/s for a total of 5 cycles. Hydrated samples were left in artificial sea water for 6-

12 and removed immediately preceding testing. Dried specimens were washed in DI water and left to dry in air at room temperature for 6-12 hours before testing. 3D printed telson cross-sectional mimics were compressed to 1 mm relative displacement at a rate of 2 μm/s. Pre-loads of 50 mN were applied to the samples to ensure contact with the parallel plate fixtures prior to testing. Biomimetic structures mimicking the 2D cross-sectional curvatures of the smasher and spearer telson were 3D printed using a desktop stereolithography printer (Form 2, FormLabs, USA) with a clear methacrylate-based photopolymer resin. CAD files of the telson cross-sectional geometries were modeled using SolidWorks (Dassault Systèmes, France). Concave and convex parts, featuring the same radius of curvature of the smasher and spearer telson dorsal cuticles, respectively, were modeled in 2-dimensions and then extruded to create a 3-dimenisonal part. A triangular truss structure was also modeled and printed as a control. All parts were designed to be the same height and depth. These files were then used for 3D printing. The 3D printed mimetic structures were compressed to 1 mm displacement, in a parallel plate configuration, at a loading rate of 2 μm/s.

Design of CAD geometries and Finite element analysis: CAD geometries used in the 3D Finite element analysis were created from the micro-CT scans of the smasher telson. The original smasher geometry was modified using tools from Geomagic (3D Systems, Morrisville, NC) to perform the necessary changes and was then exported for finite element analysis. Finite element meshes were created from the CAD files using the commercially available FEA software (ABAQUS). Simulations were performed with ABAQUS/Standard with meshes consisting of about 200,000 C3D4 elements. A linear elastic material definition was chosen with a Youngs' modulus of 1 GPa.

Powder X-ray diffraction: Powdered telson samples were prepared using a mortar and pestle. Phase identification was determined using an x-ray diffractometer (Empyrean, PANalytical, Almelo, The Nedtherlands) with Cu-Kα radiation with a generator voltage of 45 kV and tube current of 40 mA. The scan range was set from 10° to 70° (2θ).

Thermogravimetric analysis: Powdered telson samples approximately 10 mg by mass were placed in a clean alumina crucible and examined in a combination thermogravimetric/differential scanning calorimetry analyzer (SDT Q600, TA Instruments, USA) against a clean alumina reference pan. TGA/DSC were run under inert argon atmosphere with a flow rate of 100 mL/minute. The run included a 10 minute isothermal hold at room temperature followed by a ramp at 5°C/minute to 1200°C and then a steady ramp back down to room temperature.

Supporting Information

Supporting Information is available from the Wiley Online Library or from the author.

References

[1]   a) B. Achrai, H. D. Wagner, *Acta Biomater* **2013**, 9, 5890; b) I. H. Chen, J. H. Kiang, V. Correa, M. I. Lopez, P. Y. Chen, J. McKittrick, M. A. Meyers, *J Mech Behav Biomed Mater* **2011**, 4, 713; c) A. J. Clark, J. D. Triblehorn, *Peerj* **2014**, 2, e501; d) H.-O. Fabritius, S. Karsten Eva, K. Balasundaram, S. Hild, K. Huemer, D. Raabe, in *Zeitschrift für Kristallographie - Crystalline Materials*, Vol. 227, 2012, 766; e) M. A. Meyers, A. Y. Lin, P. Y. Chen, J. Muyco, *J Mech Behav Biomed Mater* **2008**, 1, 76; f) D. Raabe, C. Sachs, P. Romano, *Acta Materialia* **2005**, 53, 4281; g) V. R. Sherman, N. A. Yaraghi, D. Kisailus, M. A. Meyers, *J R Soc Interface* **2016**, 13, 20160595; h) B. Wang, W. Yang, V. R. Sherman, M. A. Meyers, *Acta Biomater* **2016**, 41, 60; i) H. Yao, M. Dao, T. Imholt, J. Huang, K. Wheeler, A. Bonilla, S. Suresh, C. Ortiz, *Proc Natl Acad Sci U S A* **2010**, 107, 987; j) E. A. Zimmermann, B. Gludovatz, E. Schaible, N. K. Dave, W. Yang, M. A. Meyers, R. O. Ritchie, *Nat Commun* **2013**, 4, 2634.

[2]   a) D. J. Emlen, *Annu Rev Ecol Evol S* **2008**, 39, 387; b) P. A. Green, S. N. Patek, *Biol Lett* **2015**, 11, 20150558; c) A. Kitchener, *Journal of Zoology* **1988**, 214, 1; d) M. E. Launey, P. Y. Chen, J. McKittrick, R. O. Ritchie, *Acta Biomater* **2010**, 6, 1505; e) B. W. Li, H. P. Zhao, X. Q. Feng, W. W. Guo, S. C. Shan, *J Exp Biol* **2010**, 213, 479; f) J.

McKittrick, P. Y. Chen, L. Tombolato, E. E. Novitskaya, M. W. Trim, G. A. Hirata, E. A. Olevsky, M. F. Horstemeyer, M. A. Meyers, *Mat Sci Eng C-Mater* **2010**, 30, 331; g) J. R. Taylor, S. N. Patek, *J Exp Biol* **2010**, 213, 3496; h) L. Tombolato, E. E. Novitskaya, P. Y. Chen, F. A. Sheppard, J. McKittrick, *Acta Biomater* **2010**, 6, 319.

[3]   a) R. L. Caldwell, *Animal Behaviour* **1979**, 27, 194; b) R. L. Caldwell, H. Dingle, *Naturwissenschaften* **1975**, 62, 214; c) J. D. Currey, A. Nash, W. Bonfield, *J. Mater. Sci.* **1982**, 17, 1939; d) S. N. Patek, R. L. Caldwell, *J Exp Biol* **2005**, 208, 3655; e) S. N. Patek, W. L. Korff, R. L. Caldwell, *Nature* **2004**, 428, 819; f) R. Steger, R. L. Caldwell, *Science* **1983**, 221, 558.

[4]   a) K. Kagaya, S. N. Patek, *J Exp Biol* **2016**, 219, 319; b) S. T. Ahyong, *Raffles B Zool* **2016**, 455.

[5]   a) W. J. Heitler, K. Fraser, E. A. Ferrero, *J Exp Biol* **2000**, 203, 183; b) E. Dahl, *Crustacean Phylogeny. Crustacean* **1983**, 189; c) R. R. Hessler, *Crustacean issues* **1983**, 1, 145.

[6]   Y. Zhang, O. Paris, N. J. Terrill, H. S. Gupta, *Sci Rep* **2016**, 6, 26249.

[7]   N. A. Yaraghi, N. Guarin-Zapata, L. K. Grunenfelder, E. Hintsala, S. Bhowmick, J. M. Hiller, M. Betts, E. L. Principe, J. Y. Jung, L. Sheppard, R. Wuhrer, J. McKittrick, P. D. Zavattieri, D. Kisailus, *Adv Mater* **2016**, 28, 6835.

[8]   C. v. Linnaeus, *Editio* **1758**, 1, 823.

[9]   a) S. Bentov, S. Abehsera, A. Sagi, in *Extracellular Composite Matrices in Arthropods*, Springer **2016**, p. 137; b) Y. Bouligand, *Tissue Cell* **1972**, 4, 189; c) P. Y. Chen, A. Y. Lin, J. McKittrick, M. A. Meyers, *Acta Biomater* **2008**, 4, 587; d) H. Fabritius, C. Sachs, D. Raabe, S. Nikolov, M. Friák, J. Neugebauer, in *Chitin*, Vol. 34 (Ed: N. S. Gupta),

Springer Netherlands **2011**, Ch. 2, p. 35; e) O. Paris, M. A. Hartmann, G. Fritz-Popovski, in *Materials Design Inspired by Nature: Function Through Inner Architecture*, DOI: 10.1039/9781849737555-00180, The Royal Society of Chemistry **2013**, p. 180.

[10]   a) P. Compère, G. Goffinet, *Tissue and Cell* **1987**, 19, 859; b) C. Sachs, H. Fabritius, D. Raabe, *J Struct Biol* **2008**, 161, 120; c) E. A. Zimmermann, R. O. Ritchie, *Advanced Healthcare Materials* **2015**, 4, 1287.

[11]   a) E. Loste, R. M. Wilson, R. Seshadri, F. C. Meldrum, *Journal of Crystal Growth* **2003**, 254, 206; b) Y. Politi, D. R. Batchelor, P. Zaslansky, B. F. Chmelka, J. C. Weaver, I. Sagi, S. Weiner, L. Addadi, *Chemistry of Materials* **2009**, 22, 161.

[12]   R. T. Downs, M. Hall-Wallace, *American Mineralogist* **2003**, 88, 247.

[13]   J. C. Weaver, G. W. Milliron, A. Miserez, K. Evans-Lutterodt, S. Herrera, I. Gallana, W. J. Mershon, B. Swanson, P. Zavattieri, E. DiMasi, D. Kisailus, *Science* **2012**, 336, 1275.

[14]   G. Cárdenas, G. Cabrera, E. Taboada, S. P. Miranda, *Journal of Applied Polymer Science* **2004**, 93, 1876.

[15]   a) P. Ammann, R. Rizzoli, *Osteoporosis International* **2003**, 14, 13; b) A. R. Palmer, G. M. Taylor, A. Barton, *Biol Bull* **1999**, 196, 281; c) H. Rahn, C. V. Paganelli, *Journal für Ornithologie* **1989**, 130, 59.

[16]   N. Suksangpanya, N. A. Yaraghi, D. Kisailus, P. Zavattieri, *J Mech Behav Biomed Mater* **2017**, 76, 38.

[17]   N. Suksangpanya, N. A. Yaraghi, R. B. Pipes, D. Kisailus, P. Zavattieri, *International Journal of Solids and Structures* **2018**, DOI: https://doi.org/10.1016/j.ijsolstr.2018.06.004.

[18]   a) R. O. Ritchie, *Nat Mater* **2011**, 10, 817; b) U. G. Wegst, H. Bai, E. Saiz, A. P. Tomsia, R. O. Ritchie, *Nat Mater* **2015**, 14, 23; c) M. E. Launey, M. J. Buehler, R. O. Ritchie, *Annual Review of Materials Research* **2010**, 40, 25.

[19]   a) I. Dayyani, A. D. Shaw, E. L. S. Flores, M. I. Friswell, *Composite Structures* **2015**, 133, 358; b) T. Yokozeki, S.-i. Takeda, T. Ogasawara, T. Ishikawa, *Composites Part A: Applied Science and Manufacturing* **2006**, 37, 1578.

[20]   L. K. Grunenfelder, N. Suksangpanya, C. Salinas, G. Milliron, N. Yaraghi, S. Herrera, K. Evans-Lutterodt, S. R. Nutt, P. Zavattieri, D. Kisailus, *Acta Biomaterialia* **2014**, 10, 3997.

[21]   N. Guarin-Zapata, J. Gomez, N. Yaraghi, D. Kisailus, P. D. Zavattieri, *Acta Biomater* **2015**, 23, 11.

[22]   R. L. Caldwell, H. Dingle, *Scientific American* **1976**, 234, 80.

[23]   a) S. T. Ahyong, *Revision of the Australian stomatopod Crustacea*, Australian Museum Sydney, **2001**; b) H. Dingle, R. L. Caldwell, *Biological Bulletin* **1978**, 155, 134.
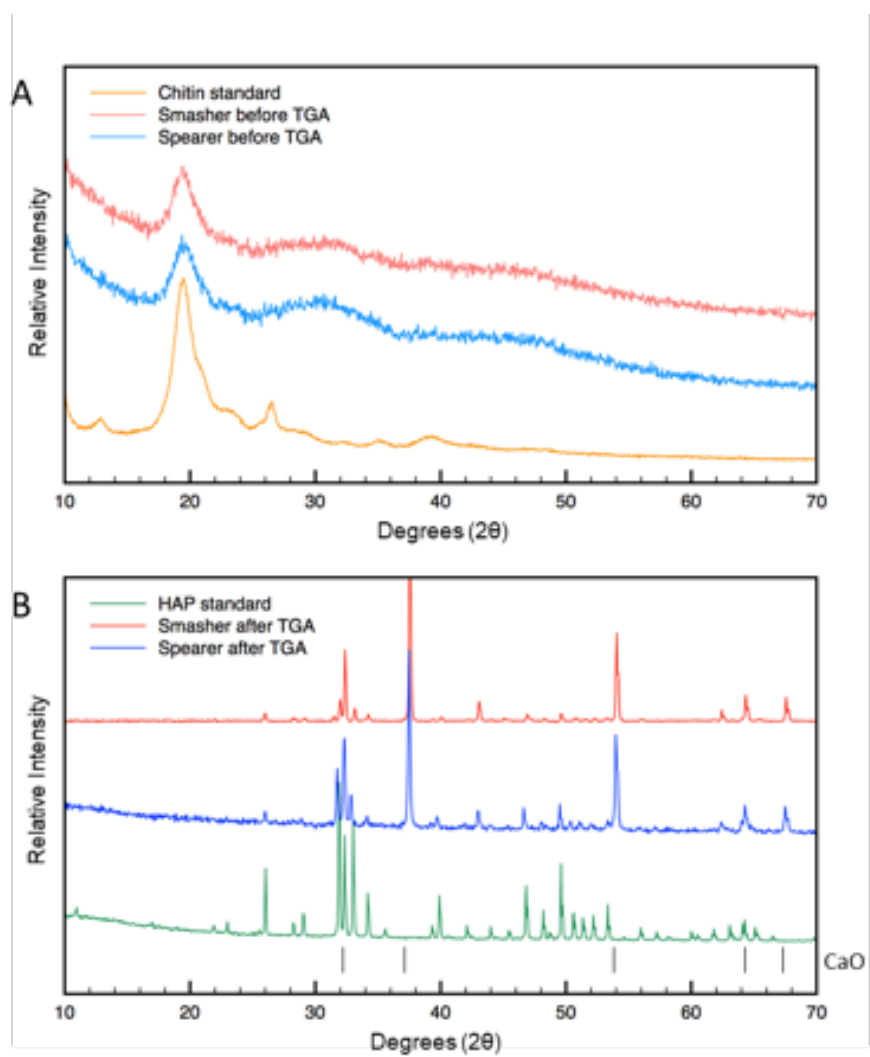
Supporting Information

Figure S1. Powder x-ray diffraction of ground smasher and spearer telson cuticle. (A) XRD spectra of intact (not annealed in a thermal gravimetric analyzer, TGA) powdered smasher and spearer telsons in addition to commercially available pure chitin. (B) XRD spectra of powdered telson samples after thermal annealing (via TGA) to 1200 °C in inert atmosphere, indicating transition to a mixture of hydroxyapatite and calcium oxide.
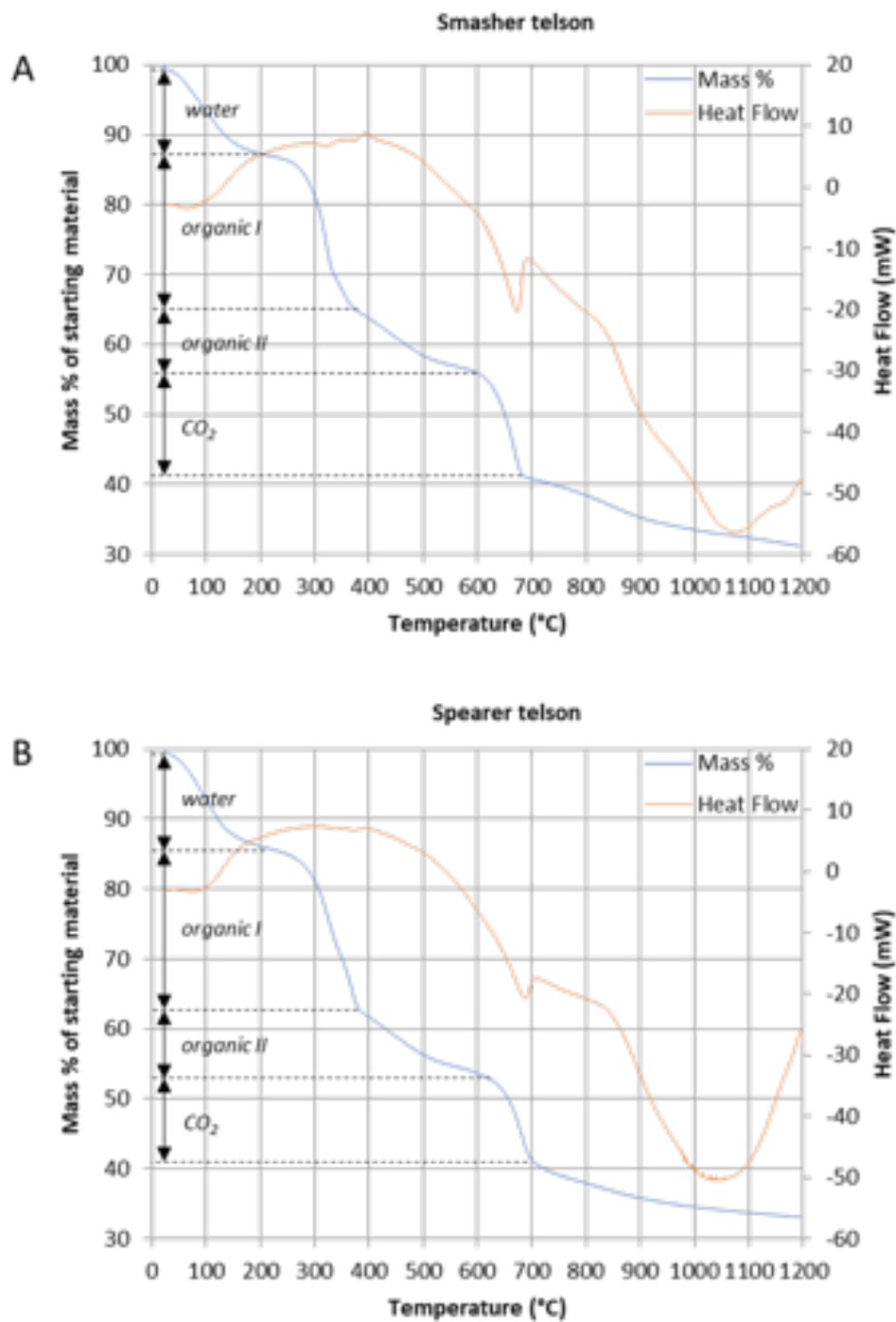
Figure S2. Thermogravimetric analysis of powdered telson samples. (A) TGA curve showing mass loss and heat flow versus temperature for a powdered smasher telson sample. (B) TGA curve showing mass loss and heat flow versus temperature for a powdered spearer telson sample.
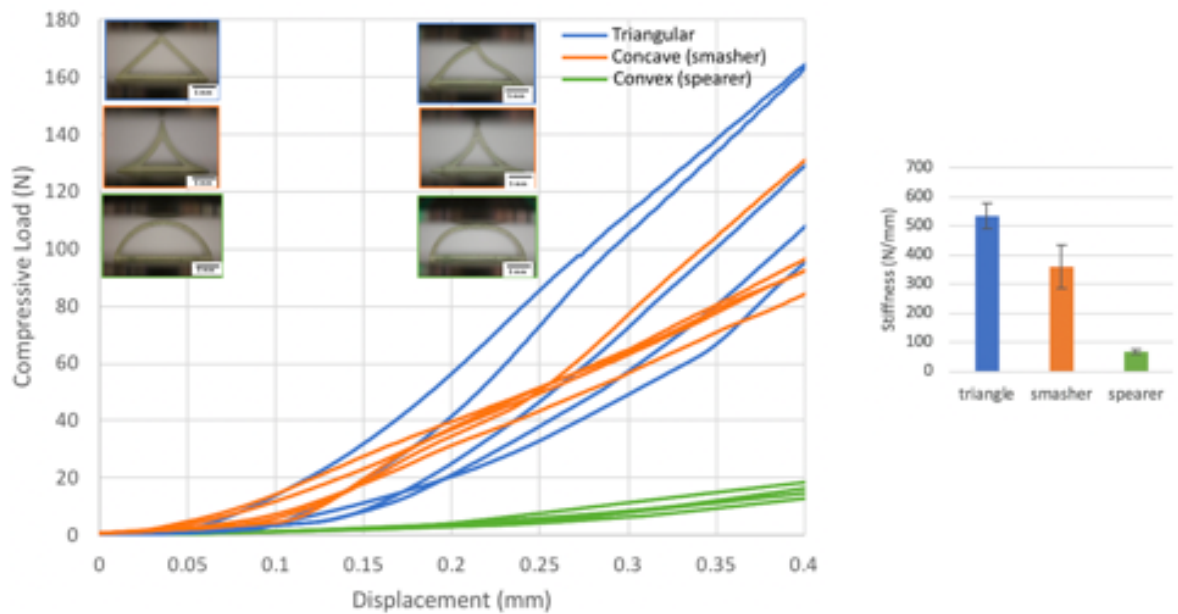
Figure S3. Compression Testing of 3D Printed Telson Geometries. Load-displacement curves showing results of compression testing on biomimetic 3D printed telson geometries. Insets show images of the triangle control (top), concave (middle), and convex (bottom) 3D printed transverse cross-sectional geometries before testing (left) and at peak load (right). Notice the buckling of the triangular and convex parts. Bar graph showing average compressive stiffness of the triangle, smasher, and spearer mimetic parts.
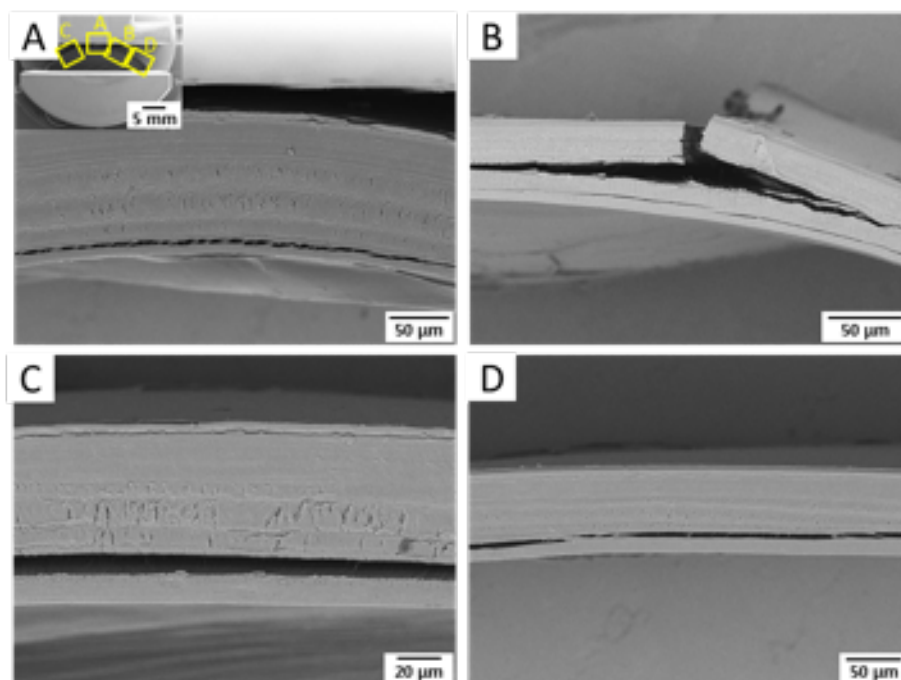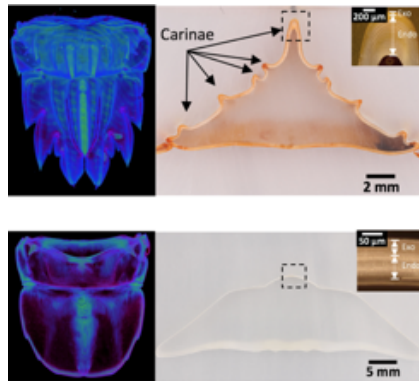
Figure S4. Ex-situ compression testing of spearer telson cross-section. (A) Low magnification BSE micrograph along the center-line of the spearer telson. Delamination within the endocuticle is apparent; however, twisting cracks are not observed. Inset showing low magnification BSE micrograph of the spearer telson cross-section loaded in the compression vice to 20% strain. (B) BSE micrograph of a lateral region of the cuticle, to the right of the center-line, showing fracture via buckling and longitudinal cracking within the endocuticle. (C, D) BSE micrographs of lateral areas of the spearer cuticle (shown in inset of (A)) showing delamination within the endocuticle and straight crack paths.

TOC:

Multi-scale structure-mechanical property relationships are identified within the shield-like exoskeletal telson structure of the mantis shrimp, used for defense and protection. Comparison of telsons from two evolutionarily divergent species reveal differences in macro-morphology, cuticle thickness, and mineralization, imparting compressive stiffness as well as compliance for energy absorption. Fibrous helicoidal micro-architectures also enhance toughening through a crack twisting mechanism.